FULL PAPER

Novel Molybdenum Carbide–Tungsten Carbide Composite Nanowires and Their Electrochemical Activation for Efficient and Stable Hydrogen Evolution

*Peng Xiao, Xiaoming Ge, Haibo Wang, Zhaolin Liu, Adrian Fisher, and Xin Wang**

Development of nonnoble metal catalysts for hydrogen evolution reaction (HER) is critical to enable an efficient production of hydrogen at low cost and large scale. In this work, a novel bimetallic carbide nanostructure consisting of Mo_2C and WC is synthesized. Based on a highly conductive WC backbone, nanosized Mo_2C particles are integrated onto WC, forming a well-defined and highly robust nanowire structure. More importantly, it is found that electrochemical activation can partially remove surface carbon and activate the catalyst by changing its surface hydrophilicity. As a result, the residual carbon contributes positively to the activity, besides its role of protecting carbide from oxidation. Benefiting from the structure, the catalyst achieves high activity, stable electrolysis towards HER.

1. Introduction

With zero carbon emission, hydrogen is envisioned as a promising energy carrier[1] to substitute for fossil fuels in future. Hydrogen production through electrochemical water-splitting has been regarded as a promising way for large scale hydrogen production on the condition that the required electricity comes from renewable energies.[2] Towards that end, the key challenge lies in the development of low-cost, highly efficient electrocatalyst to accelerate the electrochemical process of hydrogen evolution reaction (HER). Pt-group metals emerge as the most efficient candidates, but the high cost and scarce reserve on the Earth exclude the possibility of using them for practical applications. Recently, the search of nonnoble metal based catalysts reveals that some earth-abundant transition-metal sulfides,[3] selenides,[4] carbides,[5] nitrides,[6] and phosphides[7] exhibit promising electrocatalytic activities towards HER. For the well-developed MoS_x system,[8] previous efforts have been focused on the synthesis of amorphous phase,[3e,3f,9] and scaling down to nanostructured MoS_x from its bulk term, e.g., thin-layered nanoplates[10] for the benefit of the abundantly exposed S-edges. However, considering the low crystalline state of amorphous molybdenum sulfide, poor long-term stability is expected due to the possible dissolution of amorphous molybdenum sulfide back to $[MoS_4]^{2-}$ under cathodic conditions.[3e] Besides, the intrinsic low electrical conductivity of MoS_2 (10^{-8}[11] to 0.1 S cm^{-1}[12] is still a big barrier to overcome before any commercial application becomes possible. Other than sulfide, highly crystalline molybdenum carbide appears a promising candidate as it exhibits certain activity towards HER even in bulk phase[5c] and it possesses an advantageous conductivity (≈30 S cm^{-1}) over MoS_2.[13] A recent work[5e] also demonstrated that improved performance was obtained by introducing a mesoporous structure, which sheds light on greatly improving the HER performance by designing novel nanostructure and increasing surface area. Unfortunately, it is not easy to obtain controlled nanostructure as carbides are usually synthesized by high temperature carbonization process. Besides, a surface carbon layer normally forms during carbonization and subsequent activation is needed to remove this carbon layer. Such activated Mo_2C is prone to oxidation on the surface even in ambient air, as manifested by pronounced X-ray photoelectron spectroscopy (XPS) peaks[13] in high binding-energy zone, especially in aged sample. Given above, to synthesize well-defined nanostructured Mo_2C based material with superior stability in air and superb activity towards HER is still challenging and its success may truly open up a new direction for the development of nonnoble metal based electrocatalyst for water electrosplitting.

Herein, we report a novel catalyst that consists of Mo_2C and WC in a well-defined nanowire structure. Based on a tungsten trioxide precursor, molybdenum is successfully integrated onto it by a hydrothermal method. A subsequent facile carburization transforms oxide to carbide, with preserved interwoven nanowire structure. The obtained composite nanowires show excellent activity and stability towards the HER, featuring that: (1) enhanced conductivity is expected by introducing highly conductive WC as one constituent; (2) there is no need to form

P. Xiao, H. Wang, Prof. X. Wang
School of Chemical and Biomedical Engineering
Nanyang Technological University
50 Nanyang Avenue, Singapore 639798, Singapore
E-mail: WangXin@ntu.edu.sg
Dr. X. Ge, Dr. Z. Liu
Institute of Materials Research and Engineering (IMRE)
Agency of Science, Technology
and Research (A*STAR)
3 Research Link, Singapore 117602, Singapore
Prof. A. Fisher
Department of Chemical Engineering and Biotechnology
University of Cambridge
New Museums Site
Pembroke Street, Cambridge CB2 3RA, UK

DOI: 10.1002/adfm.201403633

single-layer or thin-layer nanostructure to ensure high conductivity as in the case of MoS_2; (3) nanostructured Mo_2C is integrated onto nanowire, achieving atomic affinity to WC and ensuring high structural stability; (4) electrochemical activation by cyclic voltammetry (CV) induces a hydrophilic interface of the catalyst by introducing carboxyl/epoxy groups, which facilitates the HER.

2. Results and Discussion

The well-defined nanowire structure of complex molybdenum carbide–tungsten carbide is realized by a pseudomorphic transformation of molybdenum tungsten oxide (**Scheme 1**). First, based on the knowledge that hexagonal WO_3 nanowire can be formed via a sulfate ion directing growth mechanism[14] (**Figure 1**a), adding $(NH_4)_6Mo_7O_{24}•4H_2O$ and $Na_2WO_4•2H_2O$ together in the process allows the formation of nanowires of molybdenum tungsten complex oxides, as shown in Figure 1b (W: Mo = 1:4 in molar ratio), while using $(NH_4)_6Mo_7O_{24}•4H_2O$ alone only leads to the formation of much larger microbelt of MoO_3 (not shown). To our observation, changing the molar ratio of the precursor does not lead to any morphology change as shown in Figure S1, Supporting Information (W: Mo = 1:2 in molar ratio). For the sake of convenience, the samples are termed by the nominal molar ratio of W to Mo in the precursor. The nanowires of molybdenum tungsten complex oxides in a molar ratio of 1:2 and 1:4 (W: Mo) are termed as nw-W2MoO$_3$ and nw-W4MoO$_3$, while the carbides of their counterparts are named as nw-W2MoC and nw-W4MoC respectively. After carburization, the nw-W4MoC and nw-W2MoC retain their structure of interwoven nanowires, with an average size of 15–20 nm (Figures 1c,d and S2, Supporting Information). In contrast, WC failed to retain the morphology of nanowire WO_3 and exists as interconnected particles (Figure S3, Supporting Information) and this is possibly due to the enhanced tolerance of sintering at high temperature with the addition of molybdenum. In a sense, the formation of such composite carbide nanowires is unique as a nanowire of single element carbide cannot be formed following the same approach. High magnification transmission electron microscopy (TEM) image in Figure 1e reveals that two to three layers of carbon wrap on the surface of nanowires, which is commonly detected for carbides undergoing carburization in hydrocarbons.[15] More importantly, nanoparticles of Mo_2C are found both on the surface (Figure 1e, encircled in magenta) and integrated into the nanowire structure, with highly exposed (101) planes. A uniform distribution of Mo_2C and WC is observed along the nanowires by TEM–EDX (Energy-dispersive X-ray spectroscopy) mapping in a small region in Figure 1f. The investigation of surface area through N_2 adsorption/desorption gives a Brunauer–Emmett–Teller (BET) surface area of 44 m^2 g^{-1} (Figure S4, Supporting Information) which is comparable to the mesoporous Mo_2C.[5e] But the key difference is that the surface area in this case is mostly external surface area while that from mesoporous one is mainly contributed by inner pore surfaces and is less accessible for subsequent electrochemical reaction.

The crystal structures of the samples are examined by X-ray diffraction (XRD). XRD profiles in **Figure 2**a,b indicate that single WC and Mo_2C are in hexagonal pack, indexed to space group of P-6m2 (187) and P63/mmc (194), respectively. In composite nanowires (i.e., nw-W2MoC and nw-W4MoC), hexagonal-packed Mo_2C is still present in both nw-W2MoC and nw-W4MoC, especially as a major constituent in nw-W4MoC. In contrast, hexagonal WC diminishes and gives rise to a faced-centered cubic phase. Due to the subtle difference of MoC and WC in their lattice constants (4.273 vs 4.235 Å), the cubic phase is not completely resolute at current stage. Nevertheless, what is more important is that molybdenum carbide and tungsten carbide have achieved atomic proximity in a well-defined nanowire structure. This is confirmed by the fact that the (200) of cubic carbide at 42.9° shifts to 41.6° (labeled in green dot), indicating the possible dissolution of Mo atoms into WC lattice,[5d] causing increased distance of lattice planes in the crystal structure, especially in the case of nw-W4MoC with high Mo content. To probe the surface property, XPS was employed. **Figure 3**a–c shows the typical XPS profiles of the pristine nw-W4MoC. The Mo 3d electron (Figure 3a) displays two doublets.

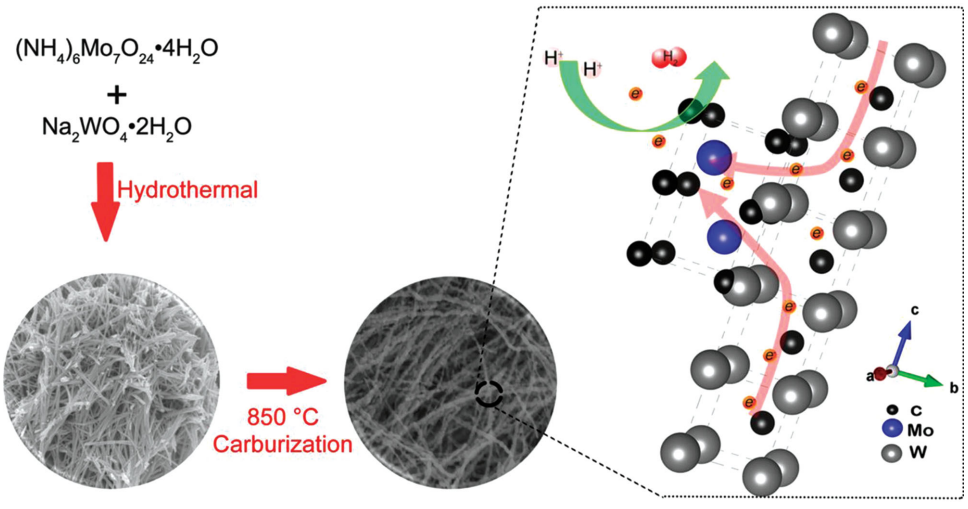

Scheme 1. Schematic formation of molybdenum carbide–tungsten carbide composite nanowires.

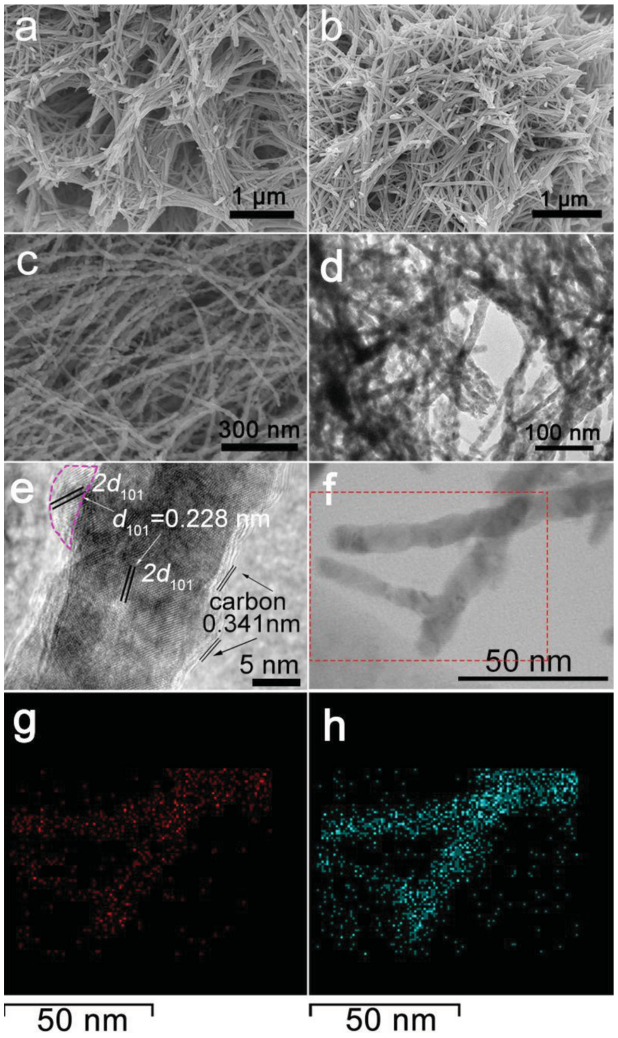

Figure 1. SEM images of the synthesized a) WO_3 nanowire, b) nw-$W4MoO_3$, c) nw-W4MoC, d)–f) TEM images of nw-W4MoC at various scales, g) Mo Kα1, and f) W Lα1: TEM–EDX mapping with respect to the area in (f).

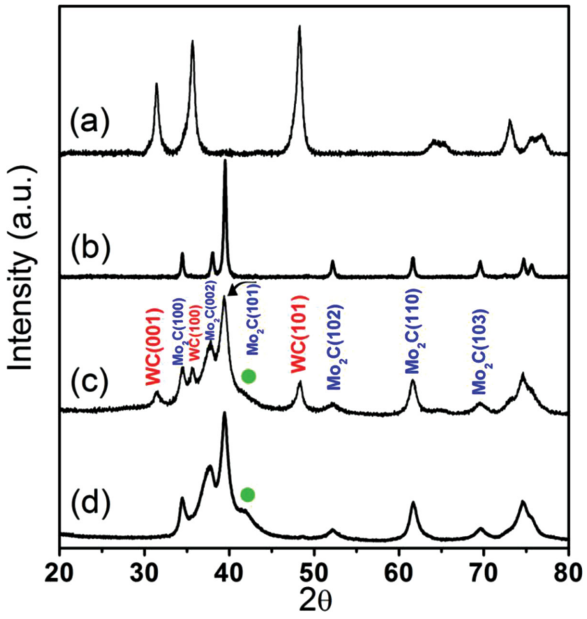

Figure 2. XRD of a) WC, b) Mo_2C, c) nw-W2MoC, and d) nw-W4MoC.

After peak deconvolution, the pair of peaks (228.8/231.9 eV) in higher binding energy is attributed to Mo^{4+} or MoO_2,[16] while the other pair is assigned to Mo_2C. No peaks representing higher valence state, e.g., Mo^{5+}, Mo^{6+}, or MoO_3, are detected. We speculate that the carbon on the surface may have prohibitive effect to prevent further oxidation, explaining the absence of the peaks Mo^{6+}/MoO_3 that is observed in our previous study of Mo_2C.[13] Similarly, W 4f electron shows strong signal in a doublet (31.5/33.65 eV) in Figure 3b, which represents the characteristic peaks for WC.[17] A small shoulder profile is also detected in the region of high binding energy (≈WO_x), indicating a minor oxidation of WC, likewise Mo_2C. However, C 1s profile only manifests the graphitic carbon ≈284.3 eV,[17] and no carbidic peak (lower binding energy, ≈282.7 eV[17] is observed. This can be ascribed to the carbon on the surface, where the graphitic carbon has covered the signal of the carbidic carbon in the similar binding energy region. Since Mo 3d and W 4f peaks are located far from C 1s peak in terms of their binding energy, it is possible to see Mo 3d and W 4f response at their binding-energy regions. A similar phenomenon is observed by Chen et al.,[17] where the graphitic carbon layers are even detectable by XRD if they are thick enough. Nevertheless, our study does not show any diffraction peaks from graphitic carbon by XRD, suggesting the thin thickness of the carbon layer.

The activities of the various catalysts are investigated in 0.5 M H_2SO_4 in a three-electrode setup (**Figure 4**). To avoid any possible contamination of Pt, carbon rod is used as the counter electrode (see the Supporting Information for the details). By comparing the catalysts synthesized, we can conclude that the activity in the pristine bimetallic carbide is higher than any single metallic carbide and such activity is mostly originated from Mo_2C,[5c,18] lying in the fact that Mo_2C obtained from commercial MoO_3 (bulk phase) outperforms WC in nanosize (Figure S3, Supporting Information) and increased content Mo from nw-W2MoC to nw-W4MoC results in improved performance (the ratio of W/Mo is determined by EDX in Figure S5, Supporting Information). Besides, possible synergistic effect between WC and Mo_2C cannot be excluded. This improved performance relative to single phase Mo_2C emphasizes the benefit of such unique structure that allows the dispersion and integration of Mo_2C in the highly conductive WC nanowire support (≈10^5 S cm^{-1} at 20 °C). Another useful metric to interpret the polarization curve is through the comparison of Tafel slope by plotting potential versus log|j| (current density in logarithm). By applying Volmer–Tafel or Volmer–Heyrovsky mechanism, Tafel slope as a descriptor gives illustrative information for the comparison of the kinetic rate of the discharging reaction (Volmer step: $H_3^+O + e^- + M \rightarrow H_{ad} - M + H_2O$[19]). Tafel slope of 82 mV dec^{-1} for WC suggests that it is inferior to Mo_2C (56 mV dec^{-1}), as shown in Figure 4b. The bimetallic carbide nanostructure does not change the reaction route, indicated by the similar Tafel slope obtained (≈56 mV dec^{-1}). In the meantime, even for the best performing catalyst (the pristine

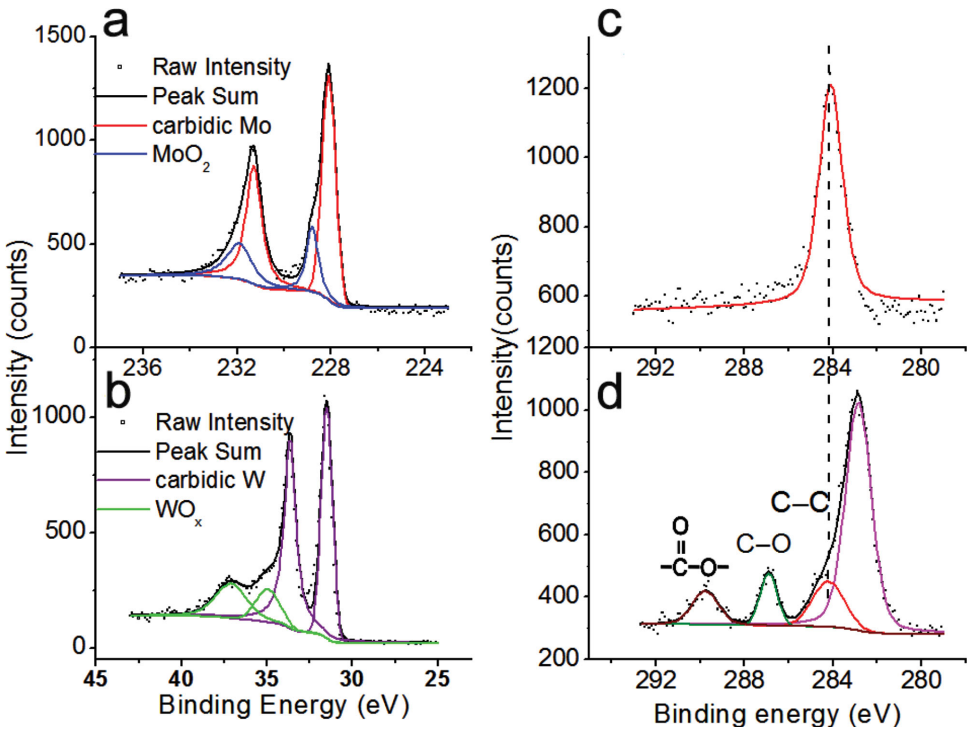

Figure 3. XPS of the nw-W4MoC sample: before activation a) Mo 3d, b) W 4f, and c) C 1s; d) after electrochemical activation C 1s.

nw-W4MoC), the overpotential after *iR* correction still reaches 250 mV at 80 mA cm^{-2} (Figure 4a). This is likely due to the presence of surface carbon layer, as evidenced from the TEM and XPS analysis. It is possible to remove the extraneous carbon by cutting off the hydrocarbon after carburization, and feeding pure H_2 immediately, but it requires the precise control of the temperature, dwell time, and hydrogen flows. Chen et al.[20] proposed the elimination of the carbon by exposing

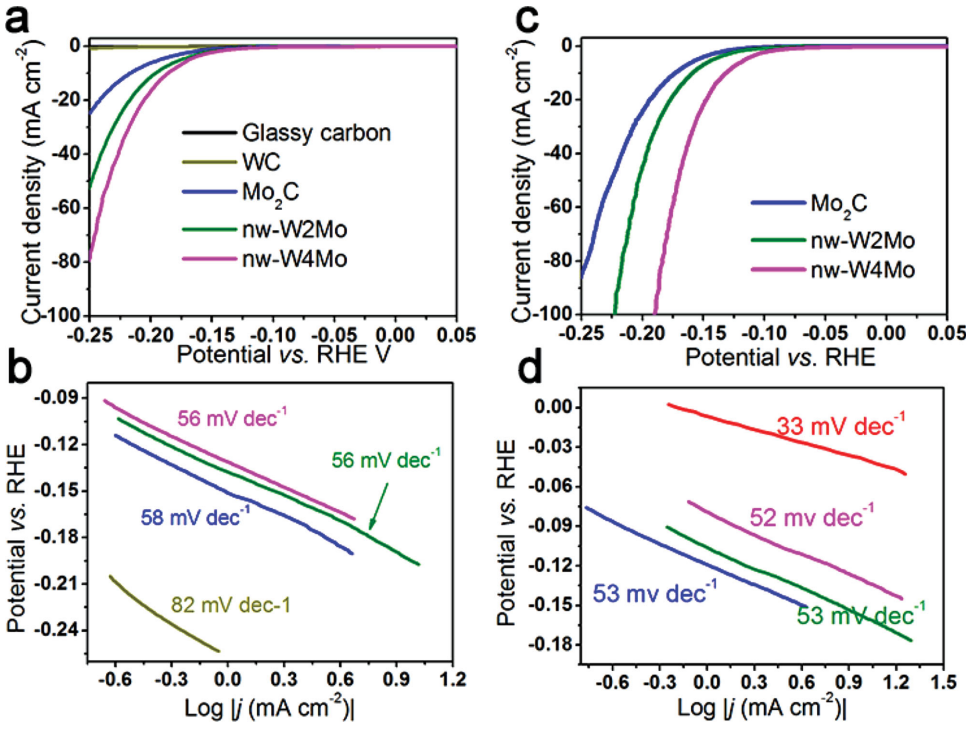

Figure 4. Polarization curves of various samples (scan rate: 2 mV s^{-1}): a) before CV activation and c) after CV activation; Tafel plots: b) before CV activation and d) after CV activation. All the curves are color-coded by referring to Figure 1a,b and red line in Figure 1d is the Tafel plot of 20% Pt/C.

Table 1. Tafel slope b and exchange current density j_o.

	Before activation		After activation	
	b [mV dec^{-1}]	j_o [mA cm^{-2}]	b [mV dec^{-1}]	j_o [mA cm^{-2}]
WC	82	6.8×10^{-4}	–	–
Mo_2C	58	2.6×10^{-3}	53	5.8×10^{-3}
nw-W2MoC	56	3.4×10^{-3}	53	1.1×10^{-2}
nw-W4MoC	56	4.7×10^{-3}	52	2.9×10^{-2}

the catalyst in an oxygen plasma environment, which requires a plasma generator. In our study, we find that simple electrochemical activation by CV (0.26–0.61 V vs RHE) could potentially serve the same purpose. Compared to the previous activation approaches, such electrochemical activation is very simple and does not need additional apparatus. The unique advantage is that it allows the in situ activation at the device level after the catalyst is assembled into the device. After the activation, significant improvement in the activity can be observed. For example, to drive a current density of 80 mA cm^{-2}, it requires an overpotential of 184 mV (vs 250 mV before activation) for the sample of nw-W4MoC and improved performance is also observed for Mo_2C and nw-W2MoC as shown in Figure 4c. The exchange current density extracted from the Tafel plot is summarized in **Table 1**, where nw-W4MoC shows five times increase in the exchange current density after the electrochemical activation (2.9×10^{-2} vs 4.7×10^{-3} mA cm^{-2}). Electrochemical impedance spectra give similar information (Figure S6 and Table S1, Supporting Information), where decreased charge transfer resistance (R_{ct}) is observed when the pristine nw-W4MoC is activated. Besides, a Tafel slope of 52 mV dec^{-1} implies that the activated nw-W4MoC is subject to the same Volmer–Heyrovsky route. To our knowledge, this performance is the best among all the carbide material investigated so far.[5] To elucidate the activation process, the activated nw-W4MoC was characterized by XPS. Figure 3d shows the profile of C 1s after the activation. In a sharp contrast to that of pristine nw-W4MoC, the peak of carbidic carbon emerges in low binding energy (282.8 eV). More importantly, oxidized forms of carbon are observed in the region of high binding energy and labeled as epoxy carbon, carboxyl group, respectively.[21] It is noteworthy that graphitic carbon is still present, but as a minor composition in the nw-W4MoC. Raman spectra in **Figure 5** evidence the graphene-like carbon in both the pristine and activated nw-W4MoC by the presence of D band and G band that is correlated with E_{2g} mode of sp^2 carbon. But the signal is less prominent after the activation. The peaks in Raman spectra around 350 and 800 cm^{-1} are from Mo_2C, representing the characteristics of Mo_2C response to Raman scattering as reported in our previous paper.[13] Given the above, the carbon layer on the surface is not completely stripped off by the CV technique. However, the electrochemical treatment successfully modified the interfacial properties by converting graphitic carbon into hydrophilic carboxyl/epoxy radicals. We intuitively propose that the negatively charged carboxyl/epoxy group may enhance the bonding to proton, and thus accelerate the diffusion of bound proton to the active site of Mo_2C, indicated by the decreased R_{ct}. This could explain the surprisingly increased

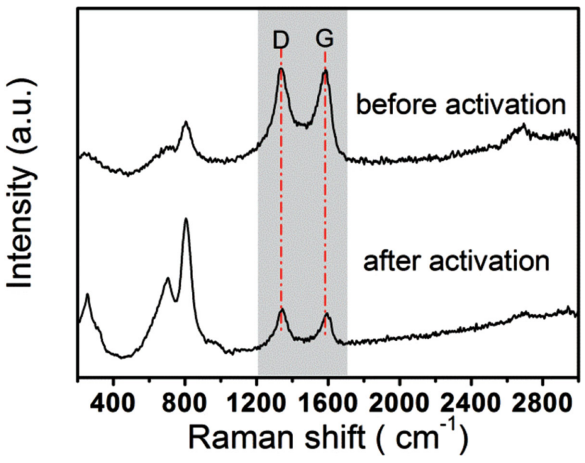

Figure 5. Raman spectra of nw-W4MoC.

performance. Given this, it would be a promising strategy that catalysts could be naturally preserved as they are freshly synthesized, and be in situ activated for performing HER by a facile CV-scan technique. The track of Mo 3d and W 4f electron through the course of activation shows that CV-scans would cause oxidation of Mo and W to high valence states (Figure S8, Supporting Information), which appears inevitable for producing the hydrophilic carboxyl groups. However, activation process via electrochemical oxidation (i.e., CV) should be conducted discreetly by choosing an appropriate potential window to avoid any severe oxidation. If the upper potential limit is too high, e.g., 0.8 V versus RHE, it would lead to severe oxidation of the carbides, resulting in decreased performance as shown in Figure S9, Supporting Information.

Stability test of the nw-W4MoC is conducted via CV between –0.2 and 0.61 V versus RHE for 3000 cycles and the stability is evaluated by comparing the polarization curves before and after the CV scan. As shown in **Figure 6**, the two polarization curves nearly overlap in low current region and only a slight decay at high current region is observed. Chronoamperometric electrolysis also demonstrates a stable hydrogen evolution for ≈20 h, indicating a good durability in an acidic environment.

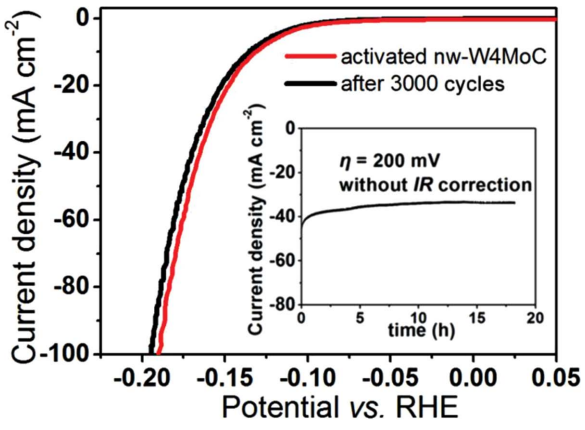

Figure 6. Stability test of the nw-W4MoC in 0.5 M H_2SO_4 with an inset graph showing chronoamperometric electrolysis.

3. Conclusions

Composite carbides consisting of Mo_2C and WC are realized in interwoven nanostructure. Nanosized Mo_2C is integrated onto highly conductive WC nanowire through a hydrothermal method, followed by a carburization route. The bimetallic carbide is demonstrated as an outstanding catalyst towards HER, showing high exchange current density, low onset potential and low charge transfer resistance. It is found that electrochemical activation can greatly enhance the activity by converting graphitic surface carbon into hydrophilic carboxyl/epoxy radicals, which produces a hydrophilic interface and ensures this outstanding performance. This work realizes the synthesis of well-defined nanostructured Mo_2C based material, and highlights the importance of surface property modulation on the electrochemical activity. This work gives emphasis on the structure–performance correlation and may potentially usher exemplary study of nonnoble metal based nanostructured catalysts for HER, by engineering the interfacial properties and designing advanced structures.

4. Experimental Section

Materials and Methods: Ammonium molybdate tetrahydrate, ($(NH_4)_6Mo_7O_{24}{\cdot}4H_2O$, Sigma-Aldrich, Bioultra, >99.0%), sodium tungstate dihydrate ($Na_2WO_4{\cdot}2H_2O$, Sigma-Aldrich, ≥99%), and ammonium sulfate ($(NH_4)_2SO_4$, Sigma-Aldrich, ≥99%) are used as received and no further purification experiments are conducted. In the hydrothermal method, stoichiometric $(NH_4)_6Mo_7O_{24}{\cdot}4H_2O$ and $Na_2WO_4{\cdot}2H_2O$ (e.g., nw-W4MoC: 0.400 g $(NH_4)_6Mo_7O_{24}{\cdot}4H_2O$, 0.184 g $Na_2WO_4{\cdot}2H_2O$ and 0.300 g $(NH_4)_2SO_4$) were dissolved in DI-water (15 mL) and adjust the pH value to ≈3 by stepwise adding HCl (5 M), followed by the hydrothermal reaction in the autoclave at 180 °C for 10 h. After washing the resulting sample collected from the autoclave, the obtained bluish powder is undergoing carburization in a gas flow of 100 s.c.c.m of 20 vol% CH_4/80 vol% H_2 in a tubular furnace at 850 °C for 1.5 h. Note that no further deactivation is needed. WC and nw-W2MoC are synthesized in the similar procedure and Mo_2C is obtained from carburizing commercial MoO_3 at the same condition.

Materials Characterization: XRD with a Cu Kα radiation source (Bruker, D2 Phaser) was used to examine the crystal structures of the as-synthesized WC, Mo_2C, nw-W2MoC, and nw-W4MoC. For Morphology, a field emission scanning electron microscope (FE–SEM, JEOL, JSM6701F, Japan), TEM (Philips CM300) coupled with Energy dispersive X-ray spectroscope (EDS) were employed. To examine the composition, X-ray photoelectron spectroscopy (XPS) experiments were performed on a VG Escalab 200i-XL spectrometer equipped with a monochromatic Al Kα (1486.6 eV) X-ray source. Electrode preparation and electrochemical measurements Raman spectroscopy spectrum was measured by a laser of 514 nm wavelength. Catalyst ink was typically made by dispersing 14 mg of catalyst in 2 mL ethanol. After adding 0.5 mL of 0.05 wt% of Nafion solution (Gashub, Singapore) and ultrasonication, an aliquot of 5 µL was pipetted onto the glassy carbon electrode (0.1963 cm^2) to reach the catalyst loading of 1.28 mg cm^{-2}. In a three-electrode configuration, Polarization curves were collected by an Autolab PGSTAT302/FRA system (Eco Chemie, Netherland) at room temperature. Carbon rod and Saturated Calomel Electrode (SCE) are used as the auxiliary electrode, the reference electrode, respectively. All the potentials shown were recorded with respect to the reversible hydrogen electrode (RHE) after *IR* correction unless it is denoted individually, where the *R* is referred to the ohmic resistance arising from the electrolyte/contact resistance of the setup, and measured by Electrochemical impedance spectroscopy (EIS) (shown in Figure S7, Supporting Information). Current density was normalized to the geometrical area of the working electrode. Polarization data are collected at the scan rate of 2 mV s^{-1} on a rotation disk electrode under 2000 rpm. EISs were carried out in a potentiostatic mode in the frequency range of 10^5 to 0.1 Hz with the amplitude of 10 mV. At different overpotentials (η = 90–120 mV with an interval of 10 mV), EIS curves were taken.

Supporting Information

Supporting Information is available from the Wiley Online Library or from the author.

Acknowledgements

This project is funded by the National Research Foundation (NRF), Prime Minister's Office, Singapore under its Campus for Research Excellence and Technological Enterprise (CREATE) programme. The authors also acknowledge financial support from the academic research fund AcRF tier 1 (M4011020 RG8/12 and M4011253 RG 7/14) Ministry of Education, Singapore.

Received: October 17, 2014
Revised: December 26, 2014
Published online: January 27, 2015

[1] J. A. Turner, *Science* **2004**, *305*, 972.
[2] M. Wang, L. Chen, L. Sun, *Energy Environ. Sci.* **2012**, *5*, 6763.
[3] a) T. F. Jaramillo, K. P. Jørgensen, J. Bonde, J. H. Nielsen, S. Horch, I. Chorkendorff, *Science* **2007**, *317*, 100; b) J. Kibsgaard, Z. Chen, B. N. Reinecke, T. F. Jaramillo, *Nat. Mater.* **2012**, *11*, 963; c) Y.-H. Chang, C.-T. Lin, T.-Y. Chen, C.-L. Hsu, Y.-H. Lee, W. Zhang, K.-H. Wei, L.-J. Li, *Adv. Mater.* **2013**, *25*, 756; d) H. Vrubel, D. Merki, X. Hu, *Energy Environ. Sci.* **2012**, *5*, 6136; e) D. Merki, S. Fierro, H. Vrubel, X. Hu, *Chem. Sci.* **2011**, *2*, 1262; f) H. Vrubel, X. Hu, *ACS Catal.* **2013**, *3*, 2002; g) H. Vrubel, T. Moehl, M. Gratzel, X. Hu, *Chem. Commun.* **2013**, *49*, 8985; h) D. Merki, X. Hu, *Energy Environ. Sci.* **2011**, *4*, 3878; i) W.-F. Chen, J. T. Muckerman, E. Fujita, *Chem. Commun.* **2013**, *49*, 8896; j) A. B. Laursen, S. Kegnaes, S. Dahl, I. Chorkendorff, *Energy Environ. Sci.* **2012**, *5*, 5577; k) Z. Wu, B. Fang, A. Bonakdarpour, A. Sun, D. P. Wilkinson, D. Wang, *Appl. Catal. B* **2012**, *125*, 59; l) T.-W. Lin, C.-J. Liu, J.-Y. Lin, *Appl. Catal. B* **2013**, *134–135*, 75; m) L. Liao, J. Zhu, X. Bian, L. Zhu, M. D. Scanlon, H. H. Girault, B. Liu, *Adv. Funct. Mater.* **2013**, *32*, 5326; n) X. Geng, W. Wu, N. Li, W. Sun, J. Armstrong, A. Al-Hilo, M. Brozak, J. Cui, T.-P. Chen, *Adv. Funct. Mater.* **2014**, *24*, 6123.
[4] a) H. Wang, D. Kong, P. Johanes, J. J. Cha, G. Zheng, K. Yan, N. Liu, Y. Cui, *Nano Lett.* **2013**, *13*, 3426; b) D. Kong, H. Wang, Z. Lu, Y. Cui, *J. Am. Chem. Soc.* **2014**, *136*, 4897; c) D. Kong, J. J. Cha, H. Wang, H. R. Lee, Y. Cui, *Energy Environ. Sci.* **2013**, *6*, 3553.
[5] a) W.-F. Chen, C. H. Wang, K. Sasaki, N. Marinkovic, W. Xu, J. T. Muckerman, Y. Zhu, R. R. Adzic, *Energy Environ. Sci.* **2013**, *6*, 943; b) W.-F. Chen, S. Iyer, S. Iyer, K. Sasaki, C.-H. Wang, Y. Zhu, J. T. Muckerman, E. Fujita, *Energy Environ. Sci.* **2013**, *6*, 1818; c) H. Vrubel, X. Hu, *Angew. Chem. Int. Ed.* **2012**, *51*, 12703; d) S. T. Hunt, T. Nimmanwudipong, Y. Román-Leshkov, *Angew. Chem. Int. Ed.* **2014**, *53*, 5131; e) L. Liao, S. Wang, J. Xiao, X. Bian, Y. Zhang, M. D. Scanlon, X. Hu, Y. Tang, B. Liu, H. H. Girault, *Energy Environ. Sci.* **2014**, *7*, 387; f) C. Wan, Y. N. Regmi, B. M. Leonard, *Angew. Chem. Int. Ed.* **2014**, *53*, 6407.
[6] a) W.-F. Chen, K. Sasaki, C. Ma, A. I. Frenkel, N. Marinkovic, J. T. Muckerman, Y. Zhu, R. R. Adzic, *Angew. Chem. Int. Ed.* **2012**,

51, 6131; b) Y. Zheng, Y. Jiao, Y. Zhu, L. H. Li, Y. Han, Y. Chen, A. Du, M. Jaroniec, S. Z. Qiao, *Nat. Commun.* **2014**, *5*, 3783.

[7] a) E. J. Popczun, J. R. Mckone, C. G. Read, A. J. Biacchi, A. M. Wiltrout, N. S. Lewis, R. E. Schaak, *J. Am. Chem. Soc.* **2013**, *135*, 9267; b) Q. Liu, J. Tian, W. Cui, P. Jiang, N. Cheng, A. M. Asiri, X. Sun, *Angew. Chem. Int. Ed.* **2014**, *53*, 6710; c) E. J. Popczun, C. G. Read, C. W. Roske, N. S. Lewis, R. E. Schaak, *Angew. Chem. Int. Ed.* **2014**, *53*, 5427; d) P. Xiao, M. A. Sk, L. Thia, X. Ge, R. J. Lim, J.-Y. Wang, K. H. Lim, X. Wang, *Energy Environ. Sci.* **2014**, *7*, 2624; e) Z. Xing, Q. Liu, A. M. Asiri, X. Sun, *Adv. Mater.* **2014**, *26*, 5702.

[8] a) C. G. Morales-Guio, L.-A. Stern, X. Hu, *Chem. Soc. Rev.* **2014**, *43*, 6555; b) Y. Yan, B. Xia, Z. Xu, X. Wang, *ACS Catal.* **2014**, *4*, 1693.

[9] J. D. Benck, Z. Chen, L. Y. Kuritzky, A. J. Forman, T. F. Jaramillo, *ACS Catal.* **2012**, *2*, 1916.

[10] a) J. Xie, J. Zhang, S. Li, F. Grote, X. Zhang, H. Zhang, R. Wang, Y. Lei, B. Pan, Y. Xie, *J. Am. Chem. Soc.* **2013**, *135*, 17881; b) J. Xie, H. Zhang, S. Li, R. Wang, X. Sun, M. Zhou, J. Zhou, X. W. Lou, Y. Xie, *Adv. Mater.* **2013**, *25*, 5807; c) Y. Yan, B. Xia, X. Ge, Z. Liu, J.-Y. Wang, X. Wang, *ACS Appl. Mater. Interfaces* **2013**, *5*, 12794.

[11] J. N. Coleman, M. Lotya, A. O'neill, S. D. Bergin, P. J. King, U. Khan, K. Young, A. Gaucher, S. De, R. J. Smith, I. V. Shvets, S. K. Arora, G. Stanton, H.-Y. Kim, K. Lee, G. T. Kim, G. S. Duesberg, T. Hallam, J. J. Boland, J. J. Wang, J. F. Donegan, J. C. Grunlan, G. Moriarty, A. Shmeliov, R. J. Nicholls, J. M. Perkins, E. M. Grieveson, K. Theuwissen, D. W. Mccomb, P. D. Nellist, V. Nicolosi, *Science* **2011**, *331*, 568.

[12] G. Eda, H. Yamaguchi, D. Voiry, T. Fujita, M. Chen, M. Chhowalla, *Nano Lett.* **2011**, *11*, 5111.

[13] P. Xiao, Y. Yan, X. Ge, Z. Liu, J.-Y. Wang, X. Wang, *Appl. Catal. B* **2014**, *154–155*, 232.

[14] Z. Gu, H. Li, T. Zhai, W. Yang, Y. Xia, Y. Ma, J. Yao, *J. Solid State Chem.* **2007**, *180*, 98.

[15] H. H. Hwu, J. G. Chen, *Chem. Rev.* **2004**, *105*, 185.

[16] a) X. Zhao, M. Cao, B. Liu, Y. Tian, C. Hu, *J. Mater. Chem.* **2012**, *22*, 13334; b) O. G. Marin Flores, S. Ha, *Appl. Catal. A* **2009**, *352*, 124.

[17] Y. C. Kimmel, D. V. Esposito, R. W. Birkmire, J. G. Chen, *Int. J. Hydrogen Energy* **2012**, *37*, 3019.

[18] T. G. Kelly, S. T. Hunt, D. V. Esposito, J. G. Chen, *Int. J. Hydrogen Energy* **2013**, *38*, 5638.

[19] J. G. N. Thomas, *Trans. Faraday Soc.* **1961**, *57*, 1603.

[20] X. Yang, Y. C. Kimmel, J. Fu, B. E. Koel, J. G. Chen, *ACS Catal.* **2012**, *2*, 765.

[21] a) J. Shen, A. Liu, Y. Tu, G. Foo, C. Yeo, M. B. Chan-Park, R. Jiang, Y. Chen, *Energy Environ. Sci.* **2011**, *4*, 4220; b) Y. Chen, B. Song, M. Li, L. Lu, J. Xue, *Adv. Funct. Mater.* **2014**, *24*, 319.